Composition and process parameter dependence of yield strength in laser powder bed fusion alloys

Hossein Eskandari Sabzi *, Pedro E.J. Rivera-Díaz-del-Castillo

Department of Engineering, Engineering Building, Lancaster University, LA1 4YW, United Kingdom

HIGHLIGHTS

- Yield stress in laser powder bed fusion described in terms of normalised enthalpy for titanium, steel and nickel alloys
- The key contribution to yield stress is the trade between dislocation multiplication and softening (Kocks-Mecking equation)
- Stainless steel maximum strength achieved with maximum heat input; titanium and nickel with reducing heat input
- Composition- and process-dependent parameters identified to maximise yield strength in laser powder bed fusion

GRAPHICAL ABSTRACT
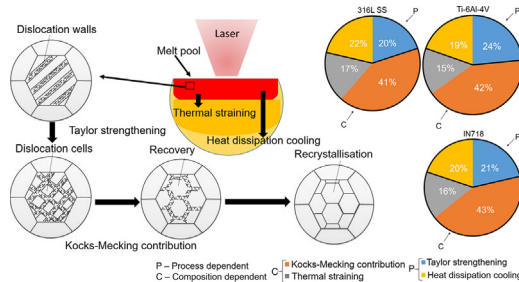
ABSTRACT

Understanding the factors influencing yield strengthening in alloys processed by laser powder bed fusion (LPBF) is critical in designing new formulations, and for predicting the optimum parameters for their processing. In this work, a relationship between the heat input and strengthening and softening mechanisms is proposed for a titanium, nickel and stainless steel alloy (Ti-6Al-4V, IN718 and 316L, respectively). Maximum strength is obtained with increasing heat input in 316L stainless steel; whereas IN718 and Ti-6Al-4V require low heat inputs. The results demonstrate that yield strength can be described in terms of the normalised enthalpy. The variation in the yield strength of LPBFed alloys depends prominently on dislocation multiplication/annihilation at certain processing temperatures and thermal straining, which are alloy dependent; as well as on dislocation strengthening and heat dissipation during cooling, which are process dependent. These dependencies are modelled via well-known metallurgical approaches. The relative contribution of various strengthening mechanisms is revealed. The findings of this work can be used as a metric for the prediction and further improvement of yield strength based on the choice of LPBF process parameters and chemical composition.

© 2020 The Authors. Published by Elsevier Ltd. This is an open access article under the CC BY license (http://creativecommons.org/licenses/by/4.0/).

1. Introduction

Laser powder bed fusion (LPBF) processing offers a good opportunity to enhance the mechanical properties of engineering alloys [1]. During LPBF, a focused laser beam selectively melts powder in thin layers to produce a solid part [2]. The most common alloy families that

* Corresponding author.

are used in LPBF are stainless steels (such as 316L stainless steel (SS)), titanium alloys (especially Ti-6Al-4V) and nickel superalloys (IN718) [3–5]. LPBF-processed alloys typically exhibit microstructures distinct from their wrought counterparts as they experience extreme heating and cooling rates and thermal strains [6]. During LPBF, the layer-by-layer scanning of a laser beam leads to a rapid non-equilibrium process [7]; this displays short interaction times between the powder and the laser beam with high heat inputs being locally applied. Sections of the powder bed experience complex cycles of heating above the melting temperature, cooling and solidification once the laser moves away, repeating this as layering proceeds. This leads to the development of solidification-enabled cellular structures, low angle grain boundaries and high dislocation densities, as well as an enhanced possibility for martensitic transformation upon cooling [8–10]; this renders most LPBF alloys exceptional strength. Representative transmission electron microscopy (TEM) micrographs of the three mentioned alloys are shown in Fig. 1. The high dislocation density resulting from dislocation multiplication/annihilation at high temperatures and thermal strains is the main feature of the LPBFed 316L SS (Fig. 1a), Ti-6Al-4V (Fig. 1b) and IN718 (Fig. 1c). The α'-martensite laths can also be seen in the microstructure of Ti-6Al-4V (Fig. 1b) as another important microstructural feature. Fig. 1d shows the cellular structure reported for as-built 316L SS [11] and Fig. 1e shows the same features inside an IN718 grain processed by LPBF [12].

A fundamental understanding of the process-structure-property relationships in engineering alloys is vital to tailor mechanical properties. There have been numerous attempts to interpret the exceptional mechanical properties of LPBF alloys [5,14–17], but variations in process parameters or chemical composition of the powder affect mechanical properties such as yield strength. Many researchers have attempted to relate them to the heat input using the energy density concept [3,18]; however, there is no specific correlation. As the material experiences multiple thermal cycles during LPBF, the heat input should play a significant role in determining the yield strength through dislocation multiplication and annihilation processes. In alloys such as 316L stainless steel (SS), dislocation climb and cross-slip readily occur. Dynamic recovery and cell formation take place at high temperatures leading to microstructural restoration [19]. In alloys in which recovery processes are slow, such as IN718, dynamic recrystallisation may set in when a critical strain is reached with new grains originating at existing grain boundaries; but for longer deformation times, further contraction causes an increase in dislocation density of certain grains [20]. The strength of alloys prone to martensitic transformation under LPBF, e.g. Ti-6Al-4V, is significantly dependent on the initial dislocation density of the parent phase at high temperatures [21]. All of the aforementioned hot deformation mechanisms can be activated during LPBF depending on the heat input. Figs. 2a-c show electron backscattered diffraction (EBSD) micrographs of as-built 316L SS reported in [8]. The orientation gradients inside the grains in an inverse pole figure (IPF) map (Fig. 2a), combined with the evolution of low angle grain boundaries (LAGBs) inside the grains (Fig. 2b) and the fact that the dislocation density is quite high, especially in coarse grains (kernel average misorientation (KAM) map shown in Fig. 2c), support the occurrence of DRV during LPBF of 316L SS. Moreover, the evolution of very fine grains with high angle grain boundaries (HAGBs) can be attributed to the activation of DRX, although this mechanism is less prominent than DRV in 316L SS. In Ti-6Al-4V, the martensite lath thickness and fraction are controlled by restoration mechanisms which determine the yield strength. A representative fine martensitic microstructure processed by LPBF is shown in Fig. 2d. The IPF map of the as-built IN718 reported in [10], is shown in Fig. 2e; this supports the presence of very fine grains, that can be attributed to the activation of DRX. The weighted contribution of the dense cellular structure (Fig. 1), and the restoration mechanisms (Fig. 2) is essential to determine the process-structure-property relationships in LPBF.

Here we present a methodology for the yield strength prediction of different types of alloys produced by LPBF. Experimental work on 316L SS, IN718 and Ti-6Al-4V demonstrates that the yield strength of
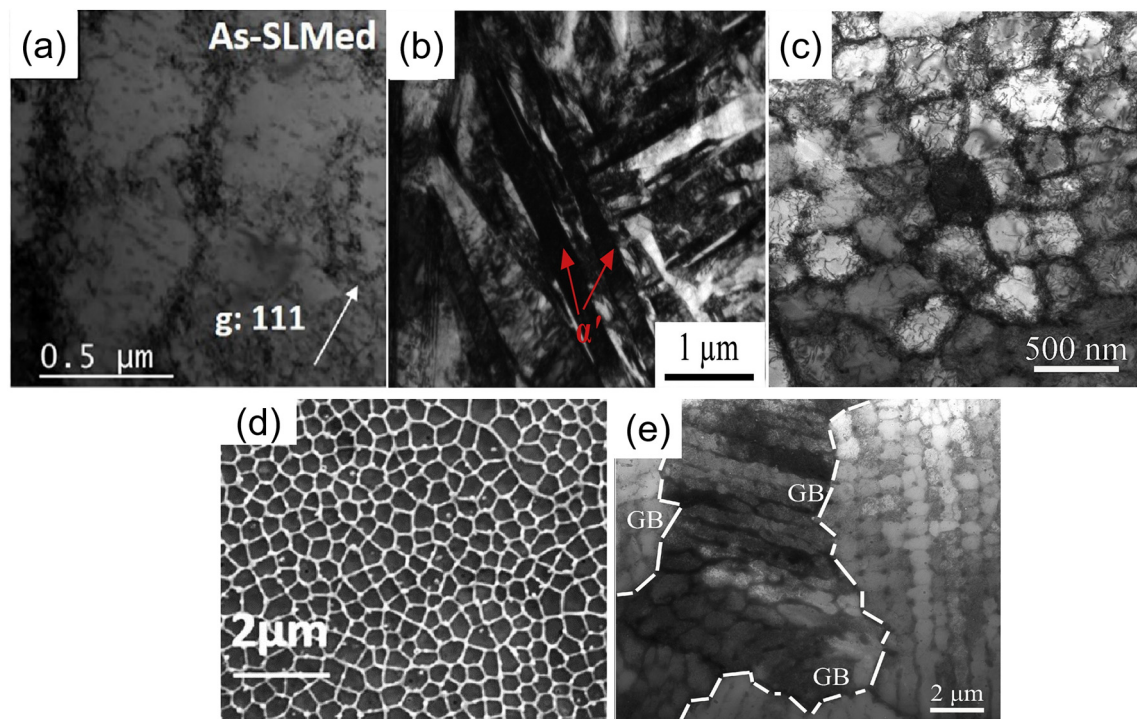

Fig. 1. The representative bright field TEM images of the LPBF processed (a) 316L SS [11], (b) Ti-6Al-4V [13] and (c) IN718 [12]. (d) Scanning electron microscope image of the microstructure of a LPBF processed 316L SS showing cellular structures [11]. (e) Bright field TEM image showing the cellular structure inside a grain (GB indicates the grain boundaries) in LPBF-processed IN718 [12].
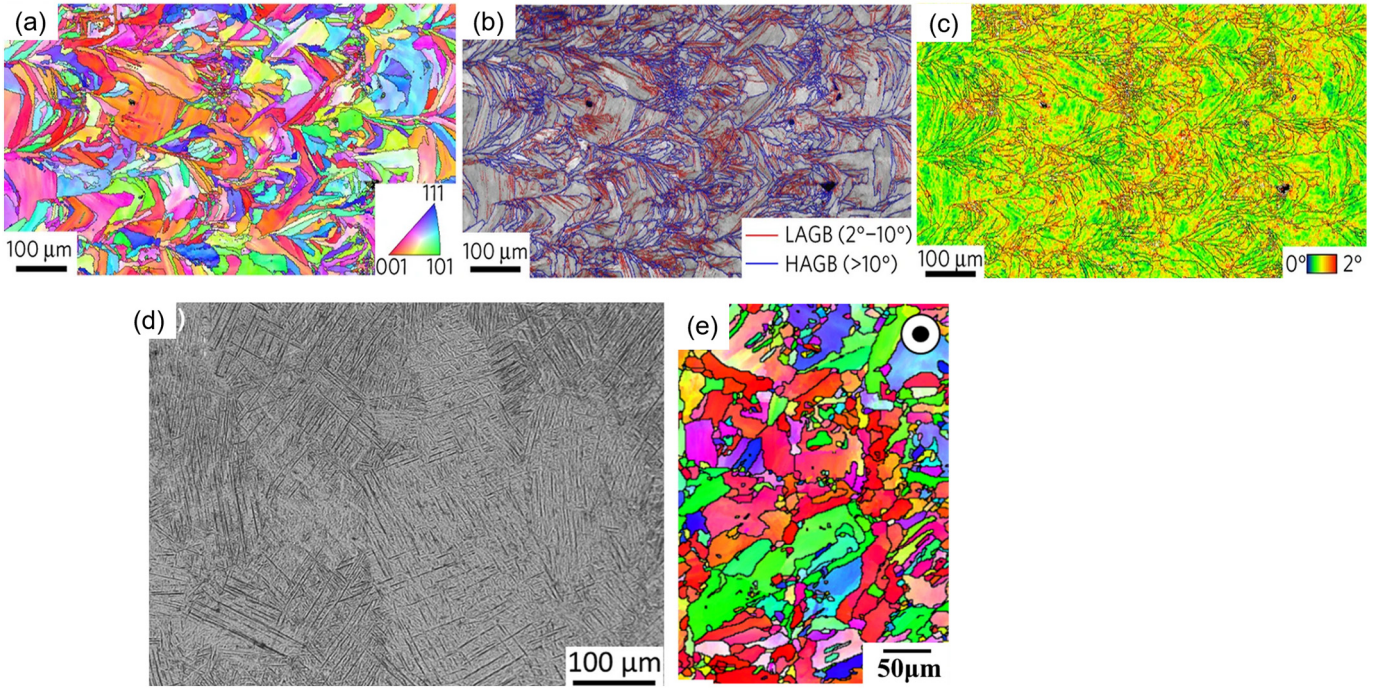
Fig. 2. (a) IPF, (b) grain boundary and (c) KAM maps for the as-built 316L SS reported in [8] (d) Optical micrograph showing fine martensite laths in an LPBFed Ti-6Al-4V [22]. (e) IPF map showing very fine grains that can be the result of activation of DRX during LPBF of IN718 [10].

as-built fully-dense LPBF specimens correlates with the heat input via the normalised enthalpy (Fig. 3). The normalised enthalpy, H_n, has been used to quantify the process heat input, which considers both the LPBF process parameters and the alloy physical properties [23]. The contribution of various mechanisms governing strengthening in LPBF alloys is revealed using analytical models. The findings presented here shed new light on the alloy and process dependent mechanisms, which can lead to maximum yield strength of LPBF alloys. This can explain some unresolved observations in the literature related to process-structure-property correlations and highlight the incompleteness of the existing single viewpoints for interpretation of the yield strength of LPBFed alloys.

2. Materials and processes

Three different alloys have been studied in this work: 316L SS, Ti-6Al-4V and IN718. H_n can be calculated via [24]:
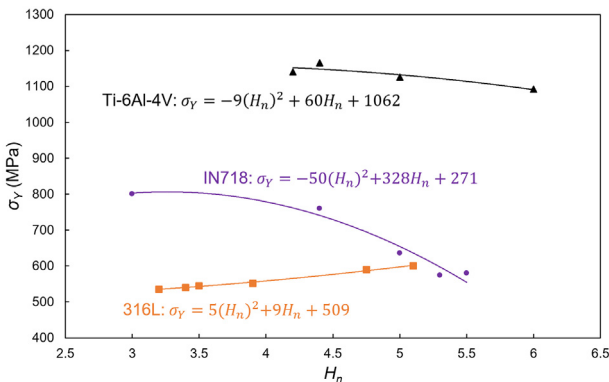

Fig. 3. Correlation between the yield strength and the normalised enthalpy H_n for alloys subjected to LPBF.

$$H_n = \frac{AP}{h_s \sqrt{\pi d v D^3}}, \tag{1}$$

where A is the absorptivity, P is the laser power, h_s is the enthalpy at the melting temperature, d is the thermal diffusivity, v is the laser scan speed and D is the nominal laser spot size. Table 1 depicts the heat input decreasing from experimental conditions 1 to 6 (E1 to E6). Experimental values of the heat input and yield strength were obtained from the literature [8,10–12,25–33] and from previous work performed by the authors [24]. The associated process parameters and materials properties for the H_n calculation are listed in Tables 2 and 3, respectively. The depicted alloys display sufficiently reduced porosity to eliminate the effects of keyholes and lack of fusion on the yield strength. The maximum H_n for keyhole formation prevention is given from [24] $H_n^{max} = \pi \frac{T_b}{T_m}$, where T_b is the boiling temperature and T_m is the melting (liquidus) temperature; therefore $H_n^{max}=$ 5.5, 6 and 6 for 316L SS, Ti-6Al-4V and IN718, respectively. The melt pool peak temperature is scaled to the boiling and melting temperatures via the ratio between H_n and H_n^{max}:

$$T_{peak} = \frac{H_n T_b}{H_n^{max}} = \frac{H_n T_m}{\pi}. \tag{2}$$

Table 1
H_n values used in this study. H_n^{max} and H_n^{min} are the limits based on boiling and melting points.

Experiment	316L H_n	Ti-6Al-4V H_n	IN718 H_n
H_n^{max}	5.5	6	6
E1	5.1 [24]	6 [25]	5.5 [26]
E2	4.75 [8]	5 [31]	5.3 [27]
E3	3.9 [11]	4.4 [33]	5 [28]
E4	3.5 [29]	4.2 [31]	4.4 [12]
E5	3.4 [30]	–	3 [10]
E6	3.2 [32]	–	–
H_n^{min}	3	3	3

Table 2
Process parameters used for H_n calculation for different materials. E1-E6 references appeared in Table 1.

Experiment	316L SS			Ti-6Al-4V			IN718		
	P (W)	v (m/s)	D (μm)	P (W)	v (m/s)	D (μm)	P (W)	v (m/s)	D (μm)
E1	100	1	35	170	0.65	100	175	0.62	100
E2	150	0.7	54	240	1	100	250	0.7	100
E3	200	0.85	70	175	0.7	100	285	1	100
E4	175	0.55	100	240	1.4	100	160	0.8	80
E5	300	0.9	100	–	–	–	400	7	100
E6	175	668	100	–	–	–	–	–	–

Table 3
Materials parameters used for solving equations in this study. The shear modulus is approximated at melting temperature. α_{CTE} values are reported values near the melting point.

Parameters	316L SS	Ti-6Al-4V	IN718
A	0.36 [24]	0.7 [34]	0.59 [35]
h_s (J/m^3)	7.76×10^9 [36]	6.15×10^9 [36]	6.81×10^9 [36]
d (m^2/s)	6×10^{-6} [24]	1.07×10^{-5} [37]	6×10^{-6} [38]
μ (Pa)	$(88{,}884.6-37.3T)\times 10^6$ [39]	$(49 - \frac{4.355}{\exp.(\frac{198}{T})-1}) \times 10^9$ [40]	$83{,}100(1-0.5\frac{(T-300)}{T_m}))\times 10^6$ [41]
b (m)	2.54×10^{-10} [42]	2.9×10^{-10} [9]	2.54×10^{-10} [43]
B	80 [44]	80.9 [45]	34 [46]
n	0.33 [44]	0.34 [45]	0.25 [46]
α_{CTE} (/K)	20.21×10^{-6} [47]	2.11×10^{-6} [48]	17.5×10^{-6} [49]
ν	0.3	0.3	0.3
η	1 [50]	1 [50]	1 [50]
k (W/m·K)	27.8 [47]	27 [51]	29.3 [52]
μ_0 (Pa)	8.88×10^{10}	49.02×10^9	8.31×10^{10}
α	0.3 [53]	0.3 [53]	0.3 [53]
T_b (K)	2885 [36]	3533 [36]	3188 [36]
T_m (K)	1648 [36]	1877 [36]	1528 [36]
c (m/s)	5280 [54]	4898 [54]	5205 [54]
E_m (J/mol)	73×10^3 [55]	121×10^3 [56]	135×10^3 [57]
C_p (J/Kg·K)	663 [36]	758 [36]	725 [36]

This is due to H_n^{max} is the maximum allowable heat input before keyhole formation, which onset is triggered by boiling [24]. The estimated T_{peak} for different conditions and materials is presented in Table 4.

To prevent lack of fusion, the lower bound to the normalised enthalpy, $H_n = H_n^{min}$, is dictated by $T_{peak} = T_m$. $H_n^{min} = \pi \approx 3$ [58] for all materials. It follows that the process boundary values are delimited by $H_n^{min} < H_n < H_n^{max}$, i.e. when the peak melt pool temperature is above melting but below boiling.

3. Theory

After tensile testing at room temperature, the relationship between yield strength and normalised enthalpy is shown in Fig. 3. There are

Table 4
Estimated values of peak temperature and strain rate during LPBF for different experimental conditions and different materials.

Experiment	T_{peak} (K)			$\dot\epsilon$ (s^{-1})		
	316L SS	Ti-6Al-4V	IN718	316L SS	Ti-6Al-4V	IN718
E1	2675	3533	2922	744	365	303
E2	2491	2944	2816	323	331	231
E3	2045	2590	2656	242	279	273
E4	1835	2473	2337	160	389	342
E5	1783	–	1594	149	–	817
E6	1678	–	–	179	–	–

multiple possible relationships between σ_Y and H_n, but the reported values are the result of a process optimisation leading to low residual stresses, low (near-full) density and a single phase upon which solidification/deformation processes are imposed. The forthcoming theory is for such process-optimised builds. In the case of 316L SS, increasing heat input results in a monotonic hardening response, whereas depending on the heat input, a balance between softening and a hardening determines the yield strength of IN718 and Ti-6Al-4V. The maximum yield strength results from the highest heat input in 316L SS. Conversely, in IN718 and Ti-6Al-4V, the maximum yield strength occurs for their lowest corresponding H_n.

Inspection of the polynomial forms of σ_Y in Fig. 3 indicate that the variation of yield stress with normalised enthalpy can be completely determined by $\frac{d\sigma_Y}{dH_n}$ and $\frac{d^2\sigma}{dH_n^2}$. The most conspicuous aspect of LPBF is rapid solidification leading to a severe thermal strain ϵ. Thus, it is postulated that $\frac{d\sigma_Y}{dH_n} = \frac{d\sigma_Y}{d\epsilon}\frac{d\epsilon}{dH_n}$, but.

- $\frac{d\epsilon}{dH_n} = \frac{d\epsilon}{dT}\frac{dT}{dH_n}$, where $\frac{d\epsilon}{dT} = \alpha_{CTE}$ is the coefficient of thermal expansion,

- and $\frac{d\sigma_Y}{d\epsilon} = \frac{d\sigma_Y}{d\rho}\frac{d\rho}{d\epsilon}$, which indicates that the thermal strain ϵ changes yield strength via a variation in dislocation density ρ.

3.1. Yield strength variation with normalised enthalpy

To reveal the contribution of the different hardening and softening mechanisms, the variation of yield strength with normalised enthalpy is therefore expressed as the product of four terms:

$$\frac{d\sigma_Y}{dH_n} = \frac{d\sigma_Y}{d\rho}\frac{d\rho}{d\epsilon}\frac{d\epsilon}{dT}\frac{dT}{dH_n}, \tag{3}$$

(i) the Taylor strengthening $\frac{d\sigma_Y}{d\rho}$, (ii) the Kocks-Mecking contribution $\frac{d\rho}{d\epsilon}$, (iii) the thermal straining $\frac{d\epsilon}{dT}$, and (iv) the heat dissipation cooling $\frac{dT}{dH_n}$. The chain rule applied in eq. (3) indicates that such variations subsequently depend on each other. In other words, for a given heat input expressed as H_n, once the laser beam moves away a temperature drop ΔT takes place, causing a unique strain inducing a variation in dislocation density that accommodates it. Based on the dislocation density obtained from the complex multiplication and annihilation processes, the yield strength can be determined via the Taylor relationship.

3.2. Yield strength variation with dislocation density

The evolution of strength is first expressed in terms of dislocation density as can be described by the well-known Taylor relationship [59]:

$$\sigma_Y = \alpha M \mu b \sqrt{\rho}, \tag{4}$$

where $\alpha = 0.3$ [53] reflects the average strength of dislocation interactions (Taylor constant), $M = 3$ [60] is the Taylor factor and accounts for textural effects, μ is the shear modulus and b is the magnitude of the Burgers vector. Therefore, the dependency of strength with dislocation density can be estimated by:

$$\frac{d\sigma_Y}{d\rho} = 0.5\alpha M \mu b \rho^{-0.5}. \tag{5}$$

For dislocation density estimation in various experimental conditions, the equations presented by Galindo-Nava et al. [61,62] are used for face-centred cubic (FCC) structures (316L SS and IN718) and body-centred cubic (BCC) structures (Ti-6Al-4V above the β-transus temperature), respectively:

$$\rho = \left[\frac{12\pi(1-\nu)}{(2+\nu)}\left(1+\frac{\eta^{-1}T\Delta S_{FCC}}{0.5\mu b^3}\right)\right]^2 d_c^{-2}, \tag{6}$$

$$\rho = \left[\frac{6\pi(1-\nu)}{(2+\nu)} \left(1 + \frac{\eta^{-1}T\Delta S_{BCC}}{2\mu b^3} \right) \right]^2 d_c^{-2}, \tag{7}$$

where ν is the Poisson's ratio, η is the impingement effect due to the overlapping strain field of contiguous dislocations that alter the possibilities for dislocation slip, ΔS_{FCC} and ΔS_{BCC} are the statistical dislocation entropies of FCC and BCC structures, respectively, T is the peak temperature and d_c is the dislocation cell size. The statistical entropy for FCC and BCC structures is respectively [62,63]:

$$\Delta S_{FCC} = k_B \ln \left(\frac{\dot{\epsilon}_0 + \vartheta}{\dot{\epsilon}} \right)^{\eta}, \tag{8}$$

$$\Delta S_{BCC} = k_B \ln \left(\frac{\dot{\epsilon}_0 + \vartheta}{\dot{\epsilon}} \right)^{2\eta}, \tag{9}$$

where k_B is the Boltzmann constant, $\dot{\epsilon}_0 = cb\rho$ is a limiting value for the strain rate, and c is the speed of sound in the bulk. $\vartheta = \vartheta_D \exp \left\{ \left(-\frac{E_m}{RT} \right) \right\}$ is the vacancy migration frequency, $\vartheta_D = 10^{13} \text{ s}^{-1}$ is the Debye frequency, $R = 8.314$ J/mol·K is the gas constant, E_m is the vacancy migration energy and T is the absolute temperature, which is taken as the peak temperature of the melt pool as in eqs. (6) and (7). ϑ accounts for the number of atomic sites a vacancy jumps per second. $\dot{\epsilon}$ is the LPBF strain rate. $\dot{\epsilon}$ can be estimated via:

$$\dot{\epsilon} = \frac{kT_{peak}v}{P}, \tag{10}$$

where k is the thermal conductivity. Eq. (10) is proposed in this work to estimate the strain rate originated by a laser beam, which speed (v) causes a maximum temperature (T_{peak}) leading to an amount of energy dissipated into the powder bed at a rate dictated by the thermal conductivity (k), but which magnitude is determined by P.

The corresponding cellular structure size (d_c) can be estimated via the average LPBF cooling rate (CR) through the empirical equation proposed by Hunt [64]:

$$d_c = B(CR)^{-n}, \tag{11}$$

where B and n are material-dependent constants. The average LPBF cooling rate can be approximated via:

$$CR = \dot{\epsilon}\Delta T, \tag{12}$$

where, ΔT is the difference between the peak temperature and the powder bed temperature.

3.3. Dislocation density variation with thermal strain

The Kocks-Mecking (KM) theory for FCC alloys (eq. (13)) and its modified version for BCC alloys (eq. (14)) have been used [62,65] to estimate the contribution of dislocation hardening and softening during LPBF:

$$\left. \frac{d\rho}{d\epsilon} \right|_{FCC} = \frac{k_1}{b} \sqrt{\rho} - f\rho, \tag{13}$$

$$\left. \frac{d\rho}{d\epsilon} \right|_{BCC} = \frac{3k_1}{8b} \sqrt{\rho} - \frac{8}{3} f\rho, \tag{14}$$

where k_1 is the dislocation storage coefficient and f is the softening coefficient, accounting for dynamic recovery and/or recrystallisation. k_1 can be estimated via $k_1 = \left(\frac{\mu}{\mu_0} \right)^2 \frac{1}{100\alpha}$ [50], where μ_0 is the shear modulus of the material at 0 K.

3.4. Thermal strain variation with temperature

The contribution of thermal strain to strengthening is constant for all conditions for a given alloy and depends only on $\alpha_{CTE} = \frac{d\epsilon}{dT}$, which values are listed in Table 3.
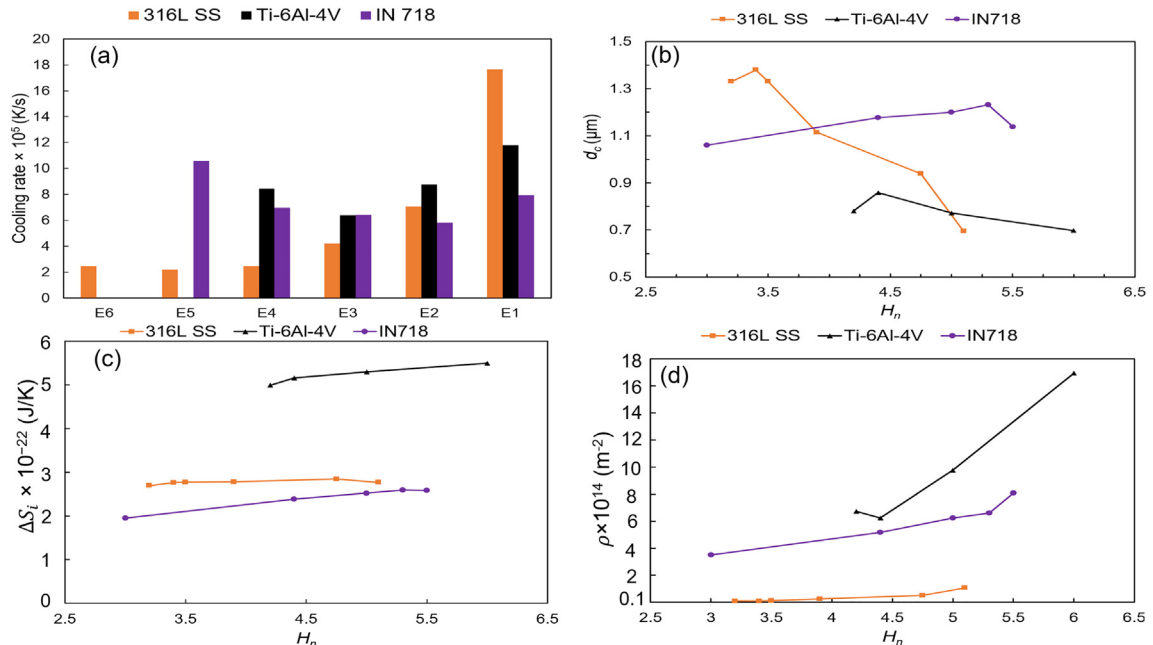

Fig. 4. (a) Average cooling rate during LPBF of different alloys under various experimental conditions. (b) Variation of dislocation cell size, (c) statistical dislocation entropy and (d) dislocation density with normalised enthalpy in different alloys.

3.5. Temperature variation with heat input

Based on eq. (1), H_n is inversely related to the enthalpy at melting h_s, which can be defined as $h_s = C_p dT + H_m$, where C_p is the heat capacity and H_m is the latent heat of fusion. Therefore, the variation of temperature with heat input can be expressed as:

$$\frac{dT}{dH_n} = -\frac{AP}{H_n^2 C_p \sqrt{\pi d v D^3}}. \tag{15}$$

4. Results

To identify the variation of yield stress with heat input, $\frac{d\sigma_Y}{dH_n}$ is calculated for 316L SS, Ti-6Al-4V and IN718. All the material properties input to calculations were collected from the literature or ThermoCalc, and are listed in Table 3, along with their sources. The contribution of dislocation density to yield strengthening in LPBF relates to the cellular structure and its corresponding dislocation cell size, which itself depends on the cooling rate. To estimate the average LPBF cooling rate for the different experimental conditions (E1-E6), the average strain rate is estimated via eq. (10) and shown in Table 4 adopting the values listed in Tables 2 and 3. Taking room temperature as the reference powder bed temperature for all experimental conditions, the average cooling rates of the different experiments are shown in Fig. 4a. The maximum strength is achieved when the cooling rate is maximum in the case of 316L SS and IN718. In contrast, the minimum cooling rate caused the maximum yield strength in Ti-6Al-4V. Using B and n values in Table 3, the dislocation cell size is estimated for various process conditions and materials (eq. 11) and is shown in Fig. 4b. In Ti-6Al-4V, which is prone to martensitic transformation upon cooling, the coarsest d_c resulted in the highest yield strength, while in non-martensitic alloys (316L SS and IN718), the finest d_c led to the maximum strength. As the dislocation density depends also on ΔS_i, i=FCC, BCC; the variation of ΔS_i with H_n for different alloys is plotted in Fig. 4c (the values in Tables 2 and 3 are used for calculations). The variation of ρ with H_n for the given heat inputs are shown in Fig. 4d.

Ti-6Al-4V displays the highest dislocation entropy and dislocation density compared with the other two alloys. 316L SS displays the lowest dislocation density. ρ increases with heat input in all cases. The contribution of dislocation density to the yield strengthening (Taylor strengthening) is shown in Fig. 5. It can be seen that Taylor strengthening has the most significant contribution to the yield strengthening in 316L SS compared with the two other alloys. There is a decrease in the
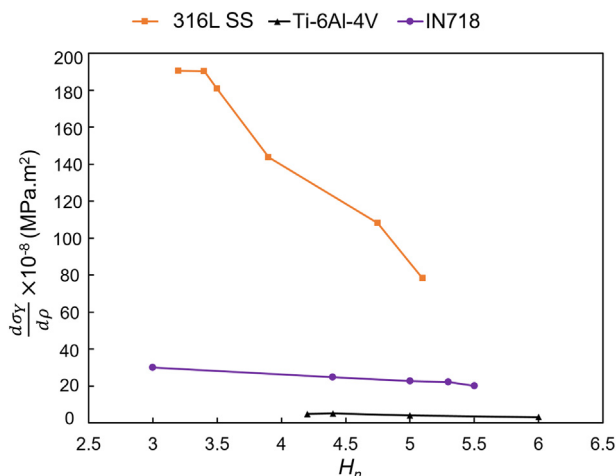
contribution of Taylor strengthening with an increase in heat input in all alloys, indicating that in 316L SS, the lower the Taylor strengthening contribution, the higher yield strength is. However, maximum yield strength is obtained when there is a highest contribution from Taylor strengthening in Ti-6Al-4V and IN718.

For solving the KM equation for the studied materials in this work, k_1 and f should be calculated. k_1 is not dependent on process parameters and heat input. However, f varies strongly with process heat input. f values are fitted to experiments and shown in Table 5. An increase in heat input results in an increase in the peak temperature, which tends to reduce f. However, the highest process temperatures increase the rate of recovery and/or recrystallisation shown in Table 6 as the softening term; this is consistent with the fact that recovery and recrystallisation are thermally activated processes, which occurrence is more likely at higher process temperatures. Table 6 indicates that increasing heat input increases both the ability for hardening and softening simultaneously. However, in 316L SS softening is more pronounced than hardening. In this material, the highest strength is obtained when softening exceeds hardening processes due to the other terms in eq. (3). But in Ti-6Al-4V hardening dominates softening; its maximum yield strength is achieved for low heat inputs, where there is a higher contribution of hardening compared with softening processes. In IN718, except for the lowest heat input, the contribution of hardening exceeds softening during LPBF. However, maximum strength is obtained when the contribution of softening dominates. The consolidated contribution of dislocation multiplication and annihilation is shown in Fig. 6. In 316L SS the more negative the KM equation value is, the higher the yield strength becomes. In Ti-6Al-4V, all the KM values are positive and the highest strengths are obtained when $\rho \varepsilon$ value is less positive at lower heat inputs. In IN718 the maximum strength is achieved when $\rho \varepsilon$ is negative (similar to 316L SS); however, in contrast with 316L SS, by increasing the heat input, the $\rho \varepsilon$ values become positive, lowering yield strength.

Taking into account that the variation of thermal strain with temperature in all cases only depends on α_{CTE}, which is independent of H_n, the final contributor to the yield strength variation with heat input is $\frac{dT}{dH_n}$, shown in Fig. 7 (computed using values reported in Tables 2 and 3). Generally, a decrease in heat input, leads to an increase in the contribution of the variations in temperature to the yield strength. Therefore, temperature variations with heat input have a more significant role in strengthening IN718 and 316L SS, compared with Ti-6Al-4V. Moreover, it can be seen that an increase in heat input results in a lower temperature drop, as increased heat enhances the melt pool stabilisation.

As a proof of concept, the numerical values associated to the product of the four terms in eq. (3) are presented as 'Model' in Fig. 8. The values directly fit from experiments, which correspond to the first derivative of the polynomial equations shown in Fig. 3, are referred to as 'Experiment' in Fig. 8:

$$\left. \frac{d\sigma_Y}{dH_n} \right|_{316LSS} = 10H_n + 9, \tag{16}$$

Fig. 5. Taylor strengthening based on the normalised enthalpy in different alloys.

Table 5
The values of k_1, f used for solving the KM type equations.

Experiment	316L SS		Ti-6Al-4V		IN718	
	k_1	f	k_1	f	k_1	f
E1	0.023	8.38	0.026	2.13	0.028	3.8
E2	0.023	11.59	0.026	2.83	0.028	4.22
E3	0.023	15.39	0.026	3.55	0.028	4.35
E4	0.023	19.39	0.026	3.42	0.028	4.78
E5	0.023	20.38	–	–	0.028	5.8
E6	0.023	20.41	–	–	–	–

Table 6
The contribution of hardening and softening during LPBF of different alloys in different processing conditions.

| Experiment	Hardening, $\frac{k_1}{b}\sqrt{\rho}$			Softening, $f\rho$		
	316L SS	Ti-6Al-4V	IN718	316L SS	Ti-6Al-4V	IN718
E1	9.799×10^{14}	3.698×10^{15}	3.150×10^{15}	9.815×10^{14}	3.620×10^{15}	3.106×10^{15}
E2	7.082×10^{14}	2.820×10^{15}	2.850×10^{15}	7.093×10^{14}	2.793×10^{15}	2.826×10^{15}
E3	5.332×10^{14}	2.260×10^{15}	2.77×10^{15}	5.337×10^{14}	2.156×10^{15}	2.752×10^{15}
E4	4.234×10^{14}	2.340×10^{15}	2.53×10^{15}	4.239×10^{14}	2.332×10^{15}	2.523×10^{15}
E5	4.025×10^{14}	–	2.095×10^{15}	4.028×10^{14}	–	2.097×10^{15}
E6	4.021×10^{14}	–	–	4.024×10^{14}	–	–
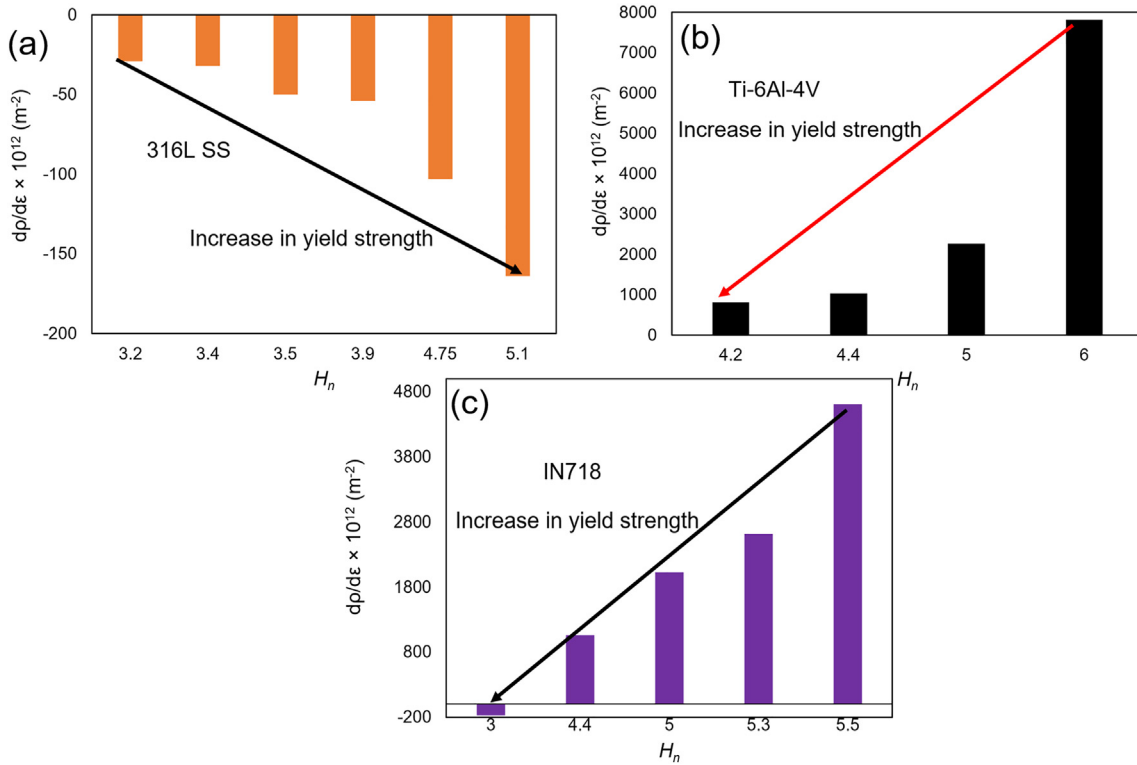
Fig. 6. Variation of dislocation density with normalised enthalpies for (a) 316L SS, (b) Ti-6Al-4V and (c) IN718.
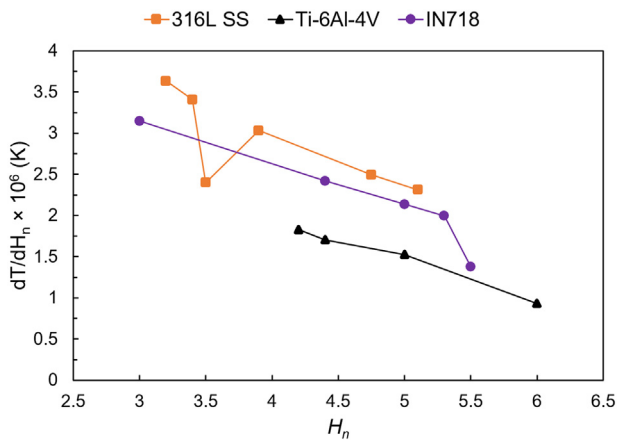

Fig. 7. The variation of temperature with normalised enthalpy during LPBF of different materials.
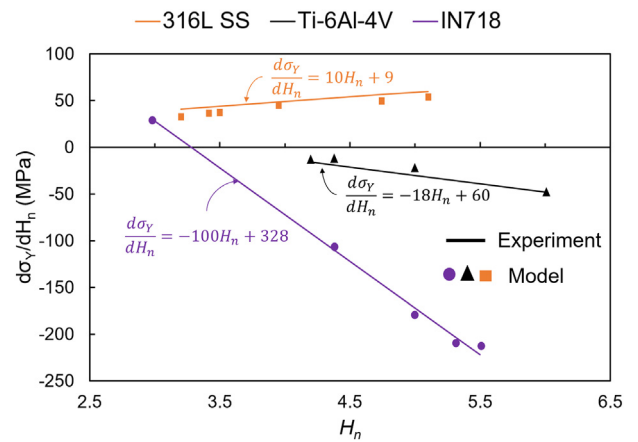

Fig. 8. Variation of the yield strength with normalised enthalpy, comparing experimental and modelling values. Eqs. (16), (17) and (18) come from the experimental fitting from Fig. 3. Model values are the product of the four numerically obtained terms in eq. (3).

$$\left.\frac{d\sigma_Y}{dH_n}\right|_{Ti-6Al-4V} = -18H_n + 60, \qquad (17)$$

$$\left.\frac{d\sigma_Y}{dH_n}\right|_{IN718} = -100H_n + 328. \qquad (18)$$

There is an excellent fit between the model and experiment in all cases. Given the near-perfect match of the slope of the curves in Fig. 8, $\frac{d^2\sigma_Y}{dH_n^2}$ can also be numerically derived, and with it the whole shape of the curves in Fig. 3 can be precisely determined in support of the validity of eq. (3).

5. Discussion

5.1. Variation of yield strength with heat input

The variation of yield strength with heat input in LPBF processed alloys depends on four mechanisms: (i) Taylor strengthening, (ii) Kocks-Mecking contribution, (iii) thermal straining and (iv) heat dissipation cooling. Taylor strengthening and heat dissipation cooling are process-dependent mechanisms, while the Kocks-Mecking contribution and thermal straining are mainly alloy-dependent mechanisms. The relative contribution of each of these mechanisms to the yield strength of different materials is illustrated in Fig. 9. We note that the vertical axis in the bar chart is $\ln\left|\frac{d\sigma_Y}{dH_n}\right| = \ln\left|\frac{d\sigma_Y}{d\rho}\right| + \ln\left|\frac{d\rho}{d\varepsilon}\right| + \ln\left|\frac{d\varepsilon}{dT}\right| + \ln\left|\frac{dT}{dH_n}\right|$ to demonstrate the relative contribution of each term in eq. (3) in the variation of yield stress with normalised enthalpy. By taking the relative contributions in the bar chart, the corresponding fractions of the contribution of each of the mechanisms are summarised in the pie charts in Fig. 9 for various alloy families.

5.2. Kocks-Mecking contribution

Kocks-Mecking contribution (Fig. 9) is the most crucial strengthening mechanism in all three different materials studied in this work, contributing to over 40% of the yield strength; but the remaining mechanisms put together play a similar role. This is in contrast with the view that the presence of the cellular structure is the only contributor to the yield strength of LPBF alloys [8,11,12,66]. Therefore, it can be concluded that the yield strength of the LPBF-produced components is significantly sensitive to the dislocation generation coefficient (k_1) and the dynamic recovery coefficient (f). From eqs. (13) and (14) it is concluded that the evolution of dislocations with the thermal strain is related to the dislocation generation and annihilation. The graphs in Fig. 6 show the Kocks-Mecking contribution to the yield strengthening. Tables 5 and 6 indicate the Kocks-Mecking contribution sensitivity and strain hardening/softening during LPBF in relation to the variations of k_1 and f. The KM equation is composed of a positive and a negative term, respectively contributing to dislocation multiplication and annihilation. A softening process (recovery/recrystallisation) at high temperatures during LPBF dominates in 316L SS, but hardening prevails in the other alloys (Fig. 6). Due to the thermal strain generated during LPBF dislocations form, and when thermal straining proceeds dislocation cross-slip and climb follows. This promotes the formation of more energy favourable dislocation cell structures with low angle grain boundaries [67]. This is part of a dynamic recovery (DRV) process, which is thought to be the main softening mechanism in 316L SS [19,39,68–70]. By increasing the dislocation population, new dislocation cells will form and grain refinement will take place that can enhance the yield strength of the material upon tensile testing [67,71]. The formation of dislocation cells during LPBF of 316L SS is in agreement with previous reports [8,11], which supports the dominance of DRV during LPBF of 316L SS. When thermal strain exceeds a certain critical value, heavily dislocated grains with dislocation cells will nucleate strain-free grains through dynamic recrystallisation (DRX), which is thought to be the main softening mechanism in LPBF of IN718 and Ti-6Al-4V [20,72].

Based on the values reported in Table 5, in 316L SS the maximum strength is obtained when f is lowest, and the highest dislocation density is achieved (Fig. 4d). 316L SS is prone to DRV; as seen in Table 6, the highest DRV rate is obtained at the highest heat input, as well as the highest contribution of the hardening term, which results in the maximum yield strength. Considering that thermal strain increases with heat input, a portion of such strain is relaxed through DRV, the rest increases dislocation density, leading to the maximum yield strength.

Ti-6Al-4V shows a completely different behaviour. The maximum strength is obtained when f is maximum and, subsequently, the
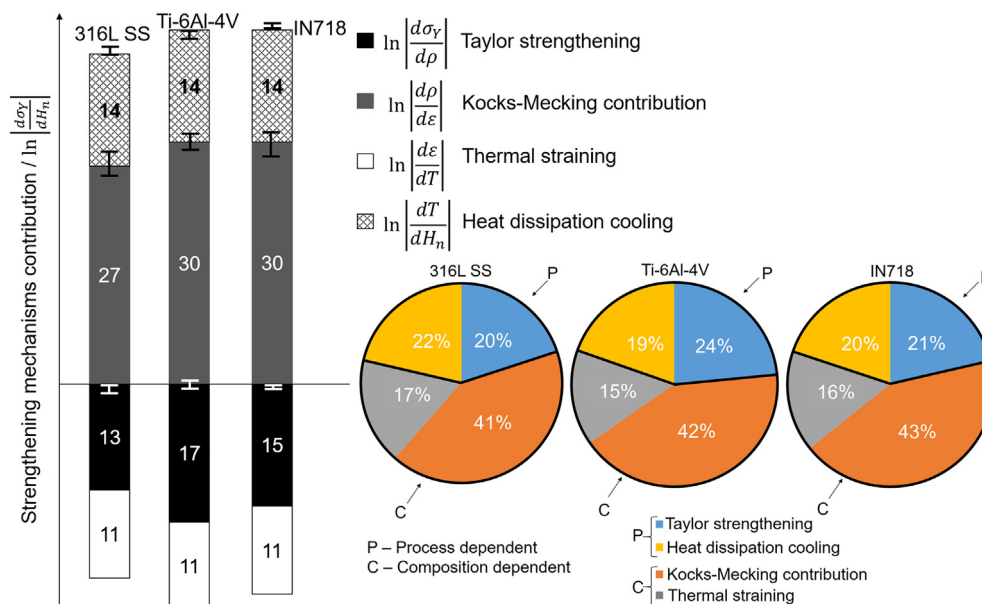

Fig. 9. Contribution of the four strengthening mechanisms involved during LPBF of different materials in a natural logarithmic scale presented in the bar chart. Error bars represent the ranges within which each term varies with H_n for the corresponding alloy. Pie charts represent the fraction of contribution of each strengthening mechanism in the alloy families produced by LPBF.

dislocation density is minimum (Fig. 4d). In Ti-6Al-4V, where DRX is thought to be the main restoration mechanism [73–76], the lower DRX rate (softening in Table 6) results in a higher tendency for martensite formation. When a critical strain for DRX is achieved, new grains form with low dislocation density [77]. This reduces the probability for martensite formation upon cooling. The thermal strain generated during LPBF in Ti-6Al-4V is estimated to be about 0.05 ($\epsilon = \alpha_{CTE}\Delta T$) in E3 and E4 conditions, and in these conditions the material has a lower ability for DRX, which leads to more martensite formation upon cooling and a higher subsequent yield strength.

Fig. 6c reveals that hardening processes dominate during LPBF of IN718 at high and moderate heat inputs (because the KM equation has a positive value). However, $\frac{d\rho}{d\epsilon}$ is negative at low heat inputs, showing the dominance of softening. IN718 is prone to DRX, when a critical strain is achieved [20,78–81]. Interestingly, the maximum strength is obtained at the lowest heat input, where softening prevails. The f values for IN718 increase with reducing heat input. However, the drop in dislocation density at low heat input, leads to a lower DRX rate at such heat inputs (Fig. 4d). The lower the rate of DRX results in the highest yield strengthening in this material.

Ti-6Al-4V and IN718 behave similarly at high temperatures (Fig. 6). It is likely that Ti-6Al-4V KM values (Fig. 6b) would become negative at lower heat inputs ($H_n \rightarrow 3$), but due to lack of data, it can be claimed that the extrapolation of the present data can lead to similar responses in Ti-6Al-4V to IN718, with both being prone to DRX during LPBF. It can be concluded that materials prone to DRX need to be processed such that the DRX rate can be slowed by reducing the softening term in KM equation. While materials prone to DRV at high temperatures should be subjected to process conditions that lead to the highest DRV rate. From Figs. 3, 316L SS yield strength increases with heat input, which is a result of higher rate of DRV during processing. However, the yield strength of Ti-6Al-4V and IN718 is determined by a balance between the softening effects of DRX and hardening of dislocation multiplication. Therefore, the reduction in DRX rate at lower heat inputs increases the yield strength in these two alloys.

5.3. Taylor strengthening

As depicted in Fig. 9, Taylor strengthening plays the second most significant role in yield strengthening of Ti-6Al-4V and IN718, while in 316L, heat dissipation cooling is more prominent. This is mostly due to the lower heat capacity (C_p) of 316L SS compared with the other studied alloys, making it more susceptible to heat dissipation upon cooling. Fig. 9 shows that, despite the fact that 316L SS has the highest Taylor strengthening values, its role in yield strengthening is even lower than heat dissipation cooling. As seen in Fig. 4d, the yield strength decreases with an increase in the dislocation density in Ti-6Al-4V and IN718. This challenges a previous point of view that yield strength is significantly controlled by the dislocation density [11,82]. Moreover, Fig. 4b indicates that the highest yield strength in Ti-6Al-4V is obtained, when the largest dislocation cell size is produced during LPBF. This also contradicts a previous hypothesis about the cruciality of dependence of yield strength on the dislocation cell size [8]. Findings of this work demonstrated that dislocation multiplication/annihilation through KM contribution dominates in determining the yield strength in LPBF processed alloys.

It is worth mentioning that the combination of a very fine dislocation cell size, which subsequently resulted in maximum dislocation density (Taylor strengthening) played as the third most significant contributor to the yield strength of 316L SS. This demonstrates that dislocation density role in strengthening is related to the cellular structure and, specifically, the size of these structures. Therefore, the cellular structure acts as a strengthening mechanism in LPBF processed 316L SS by influencing the dislocation density. For IN718, dislocation cell size directly influences the yield strengthening, without increasing the dislocation density related to cell refinement. Ti-6Al-4V has a martensitic

microstructure after it is processed by LPBF; as a very fine cellular structure can inhibit formation of martensite, the maximum yield strength is obtained when the cellular structure is coarsest, although its dislocation density is the lowest.

5.4. Heat dissipation cooling and thermal straining

The heat dissipation cooling in Ti-6Al-4V and IN718 and thermal straining in all three alloys have the lowest contribution to strengthening (Fig. 9). Fig. 7 in combination with the fact that 316L SS and IN718 have the highest thermal expansion capability caused by thermal strains, show that the yield strength in such FCC materials depends significantly on heat input values. However, martensitic materials such as Ti-6Al-4V have a lower sensitivity to variations in heat input.

5.5. Error estimation

The variability in physical properties input to eq. (1) may lead to errors in predicting the yield strength. Although the enthalpy at the melting temperature and the thermal diffusivity have fixed values for a given alloy, the absorptivity is the only parameter which measurement is sensitive to process parameters. Trapp et al. [83] showed that the LPBF process parameters can change the absorptivity values by a factor of two. They suggested the following relationship between the absorptivity and process parameters:

$$A = \frac{\Delta H \cdot vP}{l}, \tag{19}$$

where ΔH is the enthalpy and l is the total length of the laser track. Eq. (19) shows that in addition to the process parameters, the enthalpy, which can be calculated via $\Delta H = \int_{T_0}^{T_1} mC_p dT$ (where m is the mass and T_0 and T_1 are the initial and final temperatures, respectively) play a significant role. As calculation of enthalpy and determining the effective P and v values are quite challenging during LPBF, an average A has been used in eq. (1), which appears to produce reasonable results, at least in the case of keyhole and lack of fusion prevention [24]. Moreover, the two phase state during solidification of powder in LPBF makes the absorptivity measurements more challenging, supporting the use of an average A in eq. (1).

The errors caused by composition and process parameter variation in the four strengthening mechanisms introduced in this work are also shown using the error bars in Fig. 9. In all cases, the error is less than 5%.

5.6. Alloy and process design potential

Additive manufacturing technologies such as LPBF currently are using well-established wrought alloy compositions. But much effort is needed to design alloys for LPBF to exploit its unique thermo-mechanical process features. This study shows that the factors influencing the yield strength of LPBF alloys can be divided into two related categories: composition and process dependent. From an alloy design point of view, new compositions with optimised k_1 and f values can be developed to increase the yield strength of the LPBF processed alloys, via controlling process parameters to obtain the optimum dislocation cell sizes, dislocation densities and heat dissipation upon cooling. The thermostatistical approach to describe deformation is particularly suited to the task, as it naturally incorporates the effects of temperature, strain rate and composition [50,62,63,84].

The opportunities for process improvements are illustrated in Fig. 3, where significant ranges of heat input (H_n) remain unexplored, some of them likely leading to strength improvements such as $H_n < 4.2$ in Ti-6Al-4V or $H_n > 5.1$ in 316L SS.

6. Conclusions

The yield strength of fully-dense 316L stainless steel, IN718 and Ti-6Al-4V processed by LPBF is related to the process heat input, from which a methodology to describe the variation of yield strength with normalised enthalpy is proposed. Analytical models are adopted to interpret different mechanisms governing strengthening of LPBF. Taylor strengthening, Kocks-Mecking contribution, thermal straining and heat dissipation cooling are the mechanisms governing the superior mechanical properties of LPBF processed alloys. In 316L SS, high heat inputs lead to maximum strength, which is the result of a high recovery rate, combined with a higher contribution of dislocation hardening to refine the cellular structure. However, in Ti-6Al-4V and IN718, low heat inputs result in maximum strengths, which can be ascribed to a low rate of recrystallisation and a strong contribution from dislocation strengthening. The results show that dislocation multiplication/annihilation capability, which depends strongly on the composition of the alloy, controls yield strength in LPBF alloys. There is a trade between hardening resulting from dislocation multiplication and the activation of softening processes such as dynamic recovery and recrystallisation during LPBF, scaling the yield strength. Our findings provide insight into understanding the mechanisms responsible for the superior mechanical properties of different LPBF alloys. The methodology presented here, can be used as a metric for additive manufacturing community to quantify yield strength variation with process parameters and physical properties of alloy families.

Data availability

The processed data required to reproduce these findings cannot be shared at this time as the data also forms part of an ongoing study.

Credit author statement

Hossein Eskandari Sabzi performed numerical calculations, wrote paper and implemented models.

Pedro Rivera-Diaz-del-Castillo provided seminal concepts for the overall modelling and revised the manuscript.

Declaration of Competing Interest

The authors declare that they have no known competing financial interests or personal relationships that could have appeared to influence the work reported in this paper.

The authors declare the following financial interests/personal relationships which may be considered as potential competing interests:

Acknowledgments

References

[1] A. Hadadzadeh, B.S. Amirkhiz, A. Odeshi, J. Li, M. Mohammadi, Role of hierarchical microstructure of additively manufactured AlSi10Mg on dynamic loading behavior, Addit. Manuf. 28 (2019) 1–13.

[2] A. Dunbar, E. Denlinger, J. Heigel, P. Michaleris, P. Guerrier, R. Martukanitz, T.W. Simpson, Development of experimental method for in situ distortion and temperature measurements during the laser powder bed fusion additive manufacturing process, Addit. Manuf. 12 (2016) 25–30.

[3] W.E. King, A.T. Anderson, R. Ferencz, N. Hodge, C. Kamath, S.A. Khairallah, A.M. Rubenchik, Laser powder bed fusion additive manufacturing of metals; physics, computational, and materials challenges, Appl. Phys. Rev. 2 (4) (2015), 041304. .

[4] M. Masoomi, S.M. Thompson, N. Shamsaei, Laser powder bed fusion of Ti-6Al-4V parts: thermal modeling and mechanical implications, Int. J. Mach. Tools Manuf. 118 (2017) 73–90.

[5] F. Caiazzo, V. Alfieri, G. Corrado, P. Argenio, Laser powder-bed fusion of Inconel 718 to manufacture turbine blades, The. Int. J. Adv. Manuf. Tech. 93 (9–12) (2017) 4023–4031.

[6] E.R. Denlinger, M. Gouge, J. Irwin, P. Michaleris, Thermomechanical model development and in situ experimental validation of the laser powder-bed fusion process, Addit. Manuf. 16 (2017) 73–80.

[7] D.D. Gu, W. Meiners, K. Wissenbach, R. Poprawe, Laser additive manufacturing of metallic components: materials, processes and mechanisms, Int. Mater. Rev. 57 (3) (2012) 133–164.

[8] Y.M. Wang, T. Voisin, J.T. McKeown, J. Ye, N.P. Calta, Z. Li, Z. Zeng, Y. Zhang, W. Chen, T.T. Roehling, et al., Additively manufactured hierarchical stainless steels with high strength and ductility, Nat. Mater. 17 (1) (2018) 63–71.

[9] M. Galindo-Fernández, K. Mumtaz, P.E.J. Rivera-Daz-del Castillo, E.I. Galindo-Nava, H. Ghadbeigi, A microstructure sensitive model for deformation of Ti-6Al-4V describing cast-and-wrought and additive manufacturing morphologies, Mater. Des. 160 (2018) 350–362.

[10] Y.-L. Kuo, S. Horikawa, K. Kakehi, The effect of interdendritic δ phase on the mechanical properties of alloy 718 built up by additive manufacturing, Mater. Des. 116 (2017) 411–418.

[11] L. Liu, Q. Ding, Y. Zhong, J. Zou, J. Wu, Y.-L. Chiu, J. Li, Z. Zhang, Q. Yu, Z. Shen, Dislocation network in additive manufactured steel breaks strength–ductility trade-off, Mater. Today 21 (4) (2018) 354–361.

[12] T.G. Gallmeyer, S. Moorthy, B.B. Kappes, M.J. Mills, B. Amin-Ahmadi, A.P. Stebner, Knowledge of process-structure-property relationships to engineer better heat treatments for laser powder bed fusion additive manufactured Inconel 718, Addit. Manuf. 31 (2020) 100977.

[13] X. Zhao, S. Li, M. Zhang, Y. Liu, T.B. Sercombe, S. Wang, Y. Hao, R. Yang, L.E. Murr, Comparison of the microstructures and mechanical properties of Ti–6Al–4V fabricated by selective laser melting and electron beam melting, Mater. Des. 95 (2016) 21–31.

[14] Q. Zhang, J. Xie, T. London, D. Griffiths, I. Bhamji, V. Oancea, Estimates of the mechanical properties of laser powder bed fusion Ti-6Al-4V parts using finite element models, Mater. Des. 169 (2019) 107678.

[15] M. Tang, P.C. Pistorius, J.L. Beuth, Prediction of lack-of-fusion porosity for powder bed fusion, Addit. Manuf. 14 (2017) 39–48.

[16] J. Tong, C. Bowen, J. Persson, A. Plummer, Mechanical properties of titanium-based Ti–6Al–4V alloys manufactured by powder bed additive manufacture, Mater. Sci. Technol. 33 (2) (2017) 138–148.

[17] H. Fayazfar, M. Salarian, A. Rogalsky, D. Sarker, P. Russo, V. Paserin, E. Toyserkani, A critical review of powder-based additive manufacturing of ferrous alloys: process parameters, microstructure and mechanical properties, Mater. Des. 144 (2018) 98–128.

[18] T. DebRoy, H. Wei, J. Zuback, T. Mukherjee, J. Elmer, J. Milewski, A.M. Beese, A. Wilson-Heid, A. De, W. Zhang, Additive manufacturing of metallic components–process, structure and properties, Prog. Mater. Sci. 92 (2018) 112–224.

[19] E.I. Samuel, B. Choudhary, K.B.S. Rao, Influence of temperature and strain rate on tensile work hardening behaviour of type 316 LN austenitic stainless steel, Scr. Mater. 46 (7) (2002) 507–512.

[20] M. Azarbarmas, M. Aghaie-Khafri, J. Cabrera, J. Calvo, Dynamic recrystallization mechanisms and twining evolution during hot deformation of Inconel 718, Mater. Sci. Eng. A 678 (2016) 137–152.

[21] Y. Fan, P. Cheng, Y.L. Yao, Z. Yang, K. Egland, Effect of phase transformations on laser forming of Ti–6Al–4V alloy, J. Appl. Phys. 98 (1) (2005), 013518. .

[22] A.M. Beese, B.E. Carroll, Review of mechanical properties of Ti-6Al-4V made by laser-based additive manufacturing using powder feedstock, JOM. 68 (3) (2016) 724–734.

[23] H. Eskandari Sabzi, P.E.J. Rivera-Daz-del Castillo, Defect prevention in selective laser melting components: compositional and process effects, Materials 12 (22) (2019) 3791.

[24] H. Eskandari Sabzi, S. Maeng, X. Liang, M. Simonelli, N.T. Aboulkhair, P.E.J. Rivera-Daz-del Castillo, Controlling crack formation and porosity in laser powder bed fusion: alloy design and process optimisation, Addit. Manuf. 101360 (2020).

[25] H. Ali, H. Ghadbeigi, K. Mumtaz, Processing parameter effects on residual stress and mechanical properties of selective laser melted Ti6Al4V, J. Mater. Eng. Perform. 27 (8) (2018) 4059–4068.

[26] M. Aydinöz, F. Brenne, M. Schaper, C. Schaak, W. Tillmann, J. Nellesen, T. Niendorf, On the microstructural and mechanical properties of post-treated additively manufactured Inconel 718 superalloy under quasi-static and cyclic loading, Mater. Sci. Eng. A 669 (2016) 246–258.

[27] V. Popovich, E. Borisov, A. Popovich, V.S. Sufiiarov, D. Masaylo, L. Alzina, Impact of heat treatment on mechanical behaviour of Inconel 718 processed with tailored microstructure by selective laser melting, Mater. Des. 131 (2017) 12–22.

[28] H.T. Tran, Q. Chen, J. Mohan, A. C. To, A new method for predicting cracking at the interface between solid and lattice support during laser powder bed fusion additive manufacturing, Addit. Manuf. 101050 (2020).

[29] Q. Lu, N. Nguyen, A. Hum, T. Tran, C. Wong, Optical in-situ monitoring and correlation of density and mechanical properties of stainless steel parts produced by selective laser melting process based on varied energy density, J. Mater. Process. Technol. 271 (2019) 520–531.

[30] A. Wilson-Heid, T. Novak, A.M. Beese, Characterization of the effects of internal pores on tensile properties of additively manufactured austenitic stainless steel 316L, Exp. Mech. 59 (6) (2019) 793–804.

[31] C. Pauzon, P. Forêt, E. Hryha, T. Arunprasad, L. Nyborg, Argon-helium mixtures as laser-powder bed fusion atmospheres: towards increased build rate of Ti-6Al-4V, J. Mater. Process. Technol. 279 (2020) 116555.

[32] O. Salman, F. Brenne, T. Niendorf, J. Eckert, K. Prashanth, T. He, S. Scudino, Impact of the scanning strategy on the mechanical behavior of 316L steel synthesized by selective laser melting, J. Manuf. Process. 45 (2019) 255–261.

[33] A. Mertens, S. Reginster, H. Paydas, Q. Contrepois, T. Dormal, O. Lemaire, J. Lecomte-Beckers, Mechanical properties of alloy Ti–6Al–4V and of stainless steel 316L processed by selective laser melting: influence of out-of-equilibrium microstructures, Powder Metall. 57 (3) (2014) 184–189.

[34] K. Karayagiz, A. Elwany, G. Tapia, B. Franco, L. Johnson, J. Ma, I. Karaman, R. Arroyave, Numerical and experimental analysis of heat distribution in the laser powder bed fusion of Ti-6Al-4V, IISE. Trans. 51 (2) (2019) 136–152.

[35] P. Promoppatum, S.-C. Yao, P.C. Pistorius, A.D. Rollett, A comprehensive comparison of the analytical and numerical prediction of the thermal history and solidification microstructure of Inconel 718 products made by laser powder-bed fusion, Engineering. 3 (5) (2017) 685–694.

[36] J.-O. Andersson, T. Helander, L. Höglund, P. Shi, B. Sundman, Thermo-Calc & DICTRA, computational tools for materials science, CALPHAD 26 (2) (2002) 273–312.

[37] E. Soylemez, High deposition rate approach of selective laser melting through defocused single bead experiments and thermal finite element analysis for Ti-6Al-4V, Addit. Manuf. 31 (2020) 100984.

[38] P. Liu, Z. Wang, Y. Xiao, M.F. Horstemeyer, X. Cui, L. Chen, Insight into the mechanisms of columnar to equiaxed grain transition during metallic additive manufacturing, Addit. Manuf. 26 (2019) 22–29.

[39] E. Puchi Cabrera, High temperature deformation of 316L stainless steel, Mater. Sci. Technol. 17 (2) (2001) 155–161.

[40] P. Follansbee, G. Gray, An analysis of the low temperature, low and high strain-rate deformation of Ti- 6Al- 4V, Metall. Trans. A. 20 (5) (1989) 863–874.

[41] A. Thomas, M. El-Wahabi, J. Cabrera, J. Prado, High temperature deformation of Inconel 718, J. Mater. Process. Technol. 177 (1–3) (2006) 469–472.

[42] C. Robertson, M. Fivel, A. Fissolo, Dislocation substructure in 316L stainless steel under thermal fatigue up to 650 K, Mater. Sci. Eng. A 315 (1–2) (2001) 47–57.

[43] M. Fisk, J.C. Ion, L.-E. Lindgren, Flow stress model for IN718 accounting for evolution of strengthening precipitates during thermal treatment, Comput. Mater. Sci. 82 (2014) 531–539.

[44] U.S. Bertoli, B.E. MacDonald, J.M. Schoenung, Stability of cellular microstructure in laser powder bed fusion of 316l stainless steel, Mater. Sci. Eng. A 739 (2019) 109–117.

[45] M. Labudovic, R. Kovacevic, I. Kmecko, T. Khan, D. Blecic, Z. Blecic, Mechanism of surface modification of the Ti-6Al-4V alloy using a gas tungsten arc heat source, Metall. Mater. Trans. A. 30 (6) (1999) 1597–1603.

[46] S.J. Wolff, Z. Gan, S. Lin, J.L. Bennett, W. Yan, G. Hyatt, K.F. Ehmann, G.J. Wagner, W.K. Liu, J. Cao, Experimentally validated predictions of thermal history and microhardness in laser-deposited Inconel 718 on carbon steel, Addit. Manuf. 27 (2019) 540–551.

[47] W. Jiang, Y. Zhang, W. Woo, Using heat sink technology to decrease residual stress in 316L stainless steel welding joint: finite element simulation, Int. J. Press. Vessel. Pip. 92 (2012) 56–62.

[48] D.T. Queheillalt, H.N. Wadley, B.W. Choi, D.S. Schwartz, Creep expansion of porous Ti-6Al-4V sandwich structures, Metall. Mater. Trans. A. 31 (1) (2000) 261–273.

[49] D. Dye, K. Conlon, R. Reed, Characterization and modeling of quenching-induced residual stresses in the nickel-based superalloy IN718, Metall. Mater. Trans. A. 35 (6) (2004) 1703–1713.

[50] E. I. Galindo-Nava, J. Sietsma, P. E. J. Rivera-Díaz-del-Castillo, Dislocation annihilation in plastic deformation: II. kocks–mecking analysis, Acta. Mater. 60 (6–7) (2012) 2615–2624.

[51] P. Nandwana, Y. Lee, Influence of scan strategy on porosity and microstructure of Ti-6Al-4V fabricated by electron beam powder bed fusion, Mater. Today. Communications. 100962 (2020).

[52] S. Li, H. Xiao, K. Liu, W. Xiao, Y. Li, X. Han, J. Mazumder, L. Song, Melt-pool motion, temperature variation and dendritic morphology of Inconel 718 during pulsed- and continuous-wave laser additive manufacturing: a comparative study, Mater. Des. 119 (2017) 351–360.

[53] Y. Estrin, L. Toth, A. Molinari, Y. Bréchet, A dislocation-based model for all hardening stages in large strain deformation, Acta Mater. 46 (15) (1998) 5509–5522.

[54] L.M. Headings, K. Kotian, M.J. Dapino, Speed of Sound Measurement in Solids Using Polyvinylidene Fluoride (PVDF) Sensors, in: ASME 2013 Conference on Smart Materials, Adaptive Structures and Intelligent Systems, American Society of Mechanical Engineers Digital Collection, 2013.

[55] R.E. Smallman, R.J. Bishop, Modern Physical Metallurgy and Materials Engineering, Elsevier, 1999.

[56] O. Le Bacq, F. Willaime, A. Pasturel, Unrelaxed vacancy formation energies in group-iv elements calculated by the full-potential linear muffin-tin orbital method: invariance with crystal structure, Phys. Rev. B 59 (13) (1999) 8508.

[57] R.W. Cahn, P. Haasen (Eds.), Physical metallurgy 3rd revised and enlarged edition. North-Holland Physics Publishing, Amsterdam, Oxford, New York, Tokyo, 1983, Part 1 and 2.

[58] W.E. King, H.D. Barth, V.M. Castillo, G.F. Gallegos, J.W. Gibbs, D.E. Hahn, C. Kamath, A.M. Rubenchik, Observation of keyhole-mode laser melting in laser powder-bed fusion additive manufacturing, J. Mater. Process. Technol. 214 (12) (2014) 2915–2925.

[59] R. Madec, B. Devincre, L.P. Kubin, From dislocation junctions to forest hardening, Phys. Rev. Lett. 89 (25) (2002) 255508.

[60] F. Roters, D. Raabe, G. Gottstein, Work hardening in heterogeneous alloys—a microstructural approach based on three internal state variables, Acta Mater. 48 (17) (2000) 4181–4189.

[61] E.I. Galindo-Nava, P.E.J. Rivera-Díaz-del Castillo, A thermodynamic theory for dislocation cell formation and misorientation in metals, Acta Mater. 60 (11) (2012) 4370–4378.

[62] E.I. Galindo-Nava, P.E.J. Rivera-Díaz-del Castillo, Modelling plastic deformation in BCC metals: dynamic recovery and cell formation effects, Mater. Sci. Eng. A 558 (2012) 641–648.

[63] E.I. Galindo-Nava, P.E.J. Rivera-Díaz-del Castillo, Thermostatistical modelling of hot deformation in FCC metals, Int. J. Plast. 47 (2013) 202–221.

[64] J. Hunt, Solidification and Casting of Metals, the Metal Society, London 3, 1979.

[65] U. Kocks, H. Mecking, Physics and phenomenology of strain hardening: the FCC case, Prog. Mater. Sci. 48 (3) (2003) 171–273.

[66] Z. Zhu, Q. Nguyen, F. Ng, X. An, X. Liao, P. Liaw, S. Nai, J. Wei, Hierarchical microstructure and strengthening mechanisms of a CoCrFeNiMn high entropy alloy additively manufactured by selective laser melting, Scr. Mater. 154 (2018) 20–24.

[67] R. Hossain, F. Pahlevani, V. Sahajwalla, Revealing the mechanism of extraordinary hardness without compensating the toughness in a low alloyed high carbon steel, Sci. Rep. 10 (1) (2020) 1–13.

[68] B. Kashyap, K. McTaggart, K. Tangri, Study on the substructure evolution and flow behaviour in type 316L stainless steel over the temperature range 21–900 C, Philos. Mag. A. 57 (1) (1988) 97–114.

[69] S. Venugopal, S. Mannan, Y. Prasad, Processing map for hot working of stainless steel type AISI 316L, Mater. Sci. Technol. 9 (10) (1993) 899–906.

[70] B. Choudhary, Influence of strain rate and temperature on tensile deformation and fracture behavior of type 316L (N) austenitic stainless steel, Metall. Mater. Trans. A. 45 (1) (2014) 302–316.

[71] N. Ohno, J.-D. Wang, Kinematic hardening rules with critical state of dynamic recovery, part I: formulation and basic features for ratchetting behavior, Int. J. Plast. 9 (3) (1993) 375–390.

[72] H. Matsumoto, L. Bin, S.-H. Lee, Y. Li, Y. Ono, A. Chiba, Frequent occurrence of discontinuous dynamic recrystallization in Ti-6Al-4V alloy with α martensite starting microstructure, Metall. Mater. Trans. A. 44 (7) (2013) 3245–3260.

[73] R. Ding, Z. Guo, Microstructural evolution of a Ti–6Al–4V alloy during β-phase processing: experimental and simulative investigations, Mater. Sci. Eng. A 365 (1–2) (2004) 172–179.

[74] R. Ding, Z. Guo, A. Wilson, Microstructural evolution of a Ti–6Al–4V alloy during thermomechanical processing, Mater. Sci. Eng. A 327 (2) (2002) 233–245.

[75] C. Chen, J. Coyne, Deformation characteristics of Ti-6Al-4V alloy under isothermal forging conditions, Metall. Trans. A. 7 (12) (1976) 1931–1941.

[76] X. Wang, L. Wang, L. Luo, X. Liu, Y. Tang, X. Li, R. Chen, Y. Su, J. Guo, H. Fu, Hot deformation behavior and dynamic recrystallization of melt hydrogenated Ti-6Al-4V alloy, J. Alloys Compd. 728 (2017) 709–718.

[77] F.J. Humphreys, M. Hatherly, Recrystallization and Related Annealing Phenomena, Elsevier, 2012.

[78] S. Medeiros, Y. Prasad, W.G. Frazier, R. Srinivasan, Microstructural modeling of metadynamic recrystallization in hot working of IN 718 superalloy, Mater. Sci. Eng. A 293 (1–2) (2000) 198–207.

[79] M. Zouari, N. Bozzolo, R.E. Loge, Mean field modelling of dynamic and post-dynamic recrystallization during hot deformation of Inconel 718 in the absence of δ phase particles, Mater. Sci. Eng. A 655 (2016) 408–424.

[80] F.-L. Sui, L.-X. Xu, L.-Q. Chen, X.-H. Liu, Processing map for hot working of Inconel 718 alloy, J. Mater. Process. Technol. 211 (3) (2011) 433–440.

[81] J. De Jaeger, D. Solas, O. Fandeur, J.-H. Schmitt, C. Rey, 3D numerical modeling of dynamic recrystallization under hot working: application to Inconel 718, Mater. Sci. Eng. A 646 (2015) 33–44.

[82] Z. Li, B. He, Q. Guo, Strengthening and hardening mechanisms of additively manufactured stainless steels: the role of cell sizes, Scr. Mater. 177 (2020) 17–21.

[83] J. Trapp, A.M. Rubenchik, G. Guss, M.J. Matthews, In situ absorptivity measurements of metallic powders during laser powder-bed fusion additive manufacturing, Appl. Mater. Today 9 (2017) 341–349.

[84] P.E.J. Rivera-Díaz-del Castillo, K. Hayashi, E.I. Galindo-Nava, Computational design of nanostructured steels employing irreversible thermodynamics, Mater. Sci. Technol. 29 (10) (2013) 1206–1211.